CHAPTER 5

SWIFT HEAVY ION IRRADIATION OF REDUCED GRAPHENE OXIDE-POLYPYRROLE NANOTUBES NANOCOMPOSITE ELECTRODE SYSTEM

This chapter presents the effect of 85 MeV C^{6+} swift heavy ion (SHI) irradiation on the physico-chemical and electrochemical properties of 40 wt. % reduced graphene oxide-polypyrrole nanotubes nanocomposite. A systematic study of the variation in morphological, structural, thermal and electrical properties of the nanocomposite upon SHI irradiation at different fluences has been carried out by using different characterization techniques. N_2 adsorption-desorption and contact angle measurements have been conducted to investigate the surface properties of the pristine and irradiated nanocomposites. Cyclic voltammetry and galvanostatic charge-discharge measurements have been carried out to investigate the specific capacitance, energy density, power density and cycle life of the pristine and irradiated nanocomposite electrodes with different fluences. The contact and interfacial resistances of the pristine and irradiated nanocomposite electrodes have been determined using electrochemical impedance spectroscopy.

5.1 Introduction

The research on conducting polymers such as polypyrrole (PPy), polyaniline (PAni) and poly(3,4-ethylene dioxythiophene) (PEDOT) for supercapacitor electrodes have drawn great attention due to their ability to store charges by faradaic charge transfer reactions on the electrode surface known as pseudocapacitance, which yields a high specific capacitance along with good energy density [27]. However, the repeated redox reactions are limited by diffusion of ions and degrade with time resulting in poor cycle life. In this regard, carbon materials like activated carbon, carbon nanotubes and graphene have been considered as promising materials with high surface area that store charge by ion adsorption onto the electrode surface known as

electric double layer capacitance (EDLC) and exhibit a high power density and cycle life [32]. Particularly, graphene has been widely utilized as electrode materials compared to other carbonaceous materials due to its high surface-to-volume ratio along with high electrical conductivity, mechanical and thermal stability [304]. Therefore, considerable efforts have been devoted to combining conducting polymers with different carbonaceous materials to increase the power density and cycle life without sacrificing the specific capacitance and energy density [305, 306]. However, in spite of the aforesaid developments, the capacitance values are still low for real-world applications, since all the specific surface area of the electrode material is not electrochemically accessible to the electrolyte in contact. Therefore, the specific capacitance does not increase linearly with increasing specific surface area. To overcome this shortcoming, a variety of methods have been proposed to improve the capacitance by modifying the electrode surface, which includes (i) doping carbonaceous materials by hetero-atoms such as nitrogen, boron, phosphorus, and oxygen [307-310]; (ii) covalent functionalization [311]; (iii) introducing surfactants [312]; (iv) plasma treatment [313]; and (v) swift heavy ion irradiation [314].

Swift heavy ion (SHI) irradiation is a novel route to modify the properties of materials in a controlled manner at the electronic and molecular level. A wide range of SHI with different energies can be utilized to selectively tailor the structural, electrical and electrochemical properties of materials. In polymers, SHI may induce modifications like formation of new chemical bonds, intermolecular cross linking, chain scissioning or bond-breaking, fragmentation of molecules and formation of unsaturated groups [202]. The modifications are brought about by the different processes of energy loss such as nuclear and electronic energy loss of the energetic ions passing through the material as discussed in section 1.8 of Chapter 1. In SHI irradiation, the electronic energy loss dominates and the energy is transferred mainly through excitation and ionization of the atomic electrons. The coulomb explosion and thermal spike models as described in section 2.11 of Chapter 2 explain the interactions of SHI with the materials [315]. With a high electronic energy loss of about 1 to 10 keV/Å, SHI irradiation is capable of producing significant modifications and exotic effects in the materials, which is not achieved by any other means [203].

In this chapter, the reduced graphene oxide-polypyrrole nanotubes (RGO-PPyNTs) nanocomposite with 40 wt. % of RGO, which exhibited the highest electrochemical performance, has been irradiated with 85 MeV C^{6+} swift heavy ions. Irradiation of the nanocomposite has been carried out at four different fluences of 6 × 10^{10}, 3.6 × 10^{11}, 2.2 × 10^{12} and 1.3 × 10^{13} ions cm^{-2} with a view to investigate its fluence dependent electrochemical properties. The detailed procedure of SHI irradiation has been described in section 3.5 of Chapter 3. The morphological, structural and thermal properties of the pristine (unirradiated) and irradiated nanocomposites with different fluences have been investigated by FESEM, HRTEM, XRD, FTIR, micro-Raman and thermogravimetric analysis. Electrical and surface characterizations of the nanocomposites upon irradiation have been performed by two-probe I-V, four-probe conductivity, contact angle and N_2 adsorption-desorption measurements and compared with that of the pristine nanocomposite. The electrochemical performance parameters such as specific capacitance, energy density, power density and coulombic efficiency of the nanocomposites have been determined before and after irradiation with different fluences by cyclic voltammetry, galvanostatic charge-discharge and electrochemical impedance spectroscopy. The cyclic stability of the pristine and SHI irradiated 40 wt. % RGO-PPyNTs nanocomposites has been studied for 1000 cycles.

5.2 Structural characterization

5.2.1 Morphological analysis

The FESEM images of pristine and SHI irradiated 40 wt. % RGO-PPyNTs nanocomposites are shown in Figure 5.1.

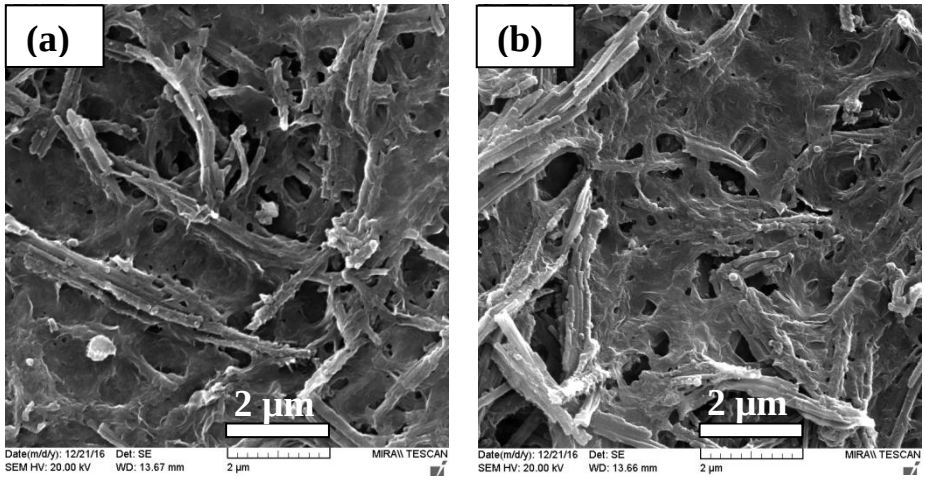

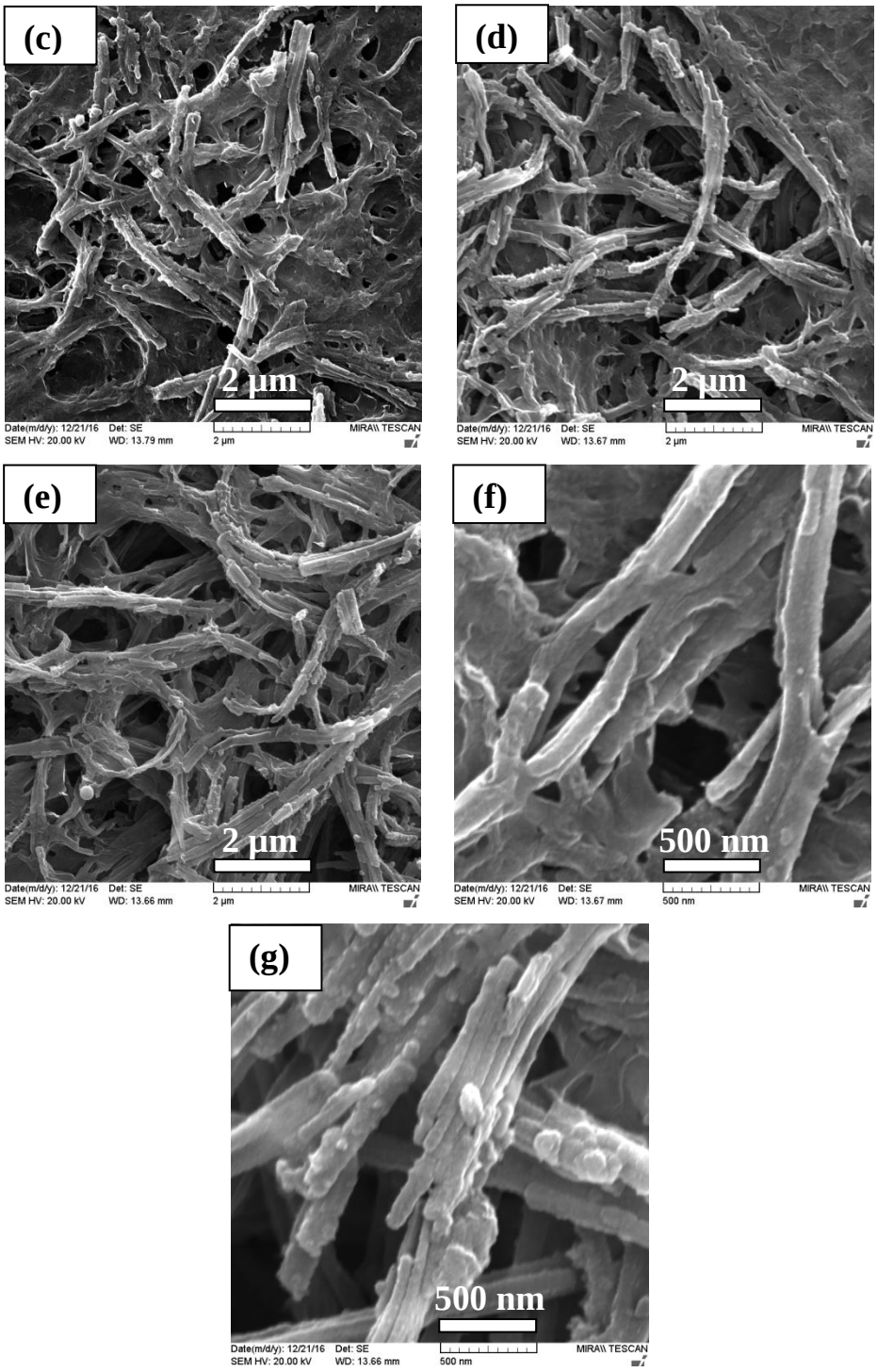

Figure 5.1: *FESEM images of 40 wt. % RGO-PPyNTs nanocomposite (a) pristine, and irradiated with fluence of (b) 6 × 10^{10}, (c) 3.6 × 10^{11}, (d) 2.2 × 10^{12}, (e) 1.3 × 10^{13} ions cm^{-2} at a magnification of 25 kx; FESEM images of 40 wt. % RGO-PPyNTs nanocomposite (f) pristine, and irradiated with fluence of (g) 1.3 × 10^{13} ions cm^{-2} at a magnification of 100 kx.*

The images after irradiation reveal the widening of pores on the surface of the nanocomposite electrode. The pores are not so significant up to a fluence of 6×10^{10} ions cm^{-2}. However on increasing the SHI fluence, the pore size increases showing a broad distribution profile in the range of 0.41-2.18 μm from a fluence of 3.6×10^{11} to 1.3×10^{13} ions cm^{-2}. SHI irradiation produces large electronic energy loss, which causes excitation and ionization of electrons of the target material resulting in the formation of defects and structural damage at the ion impact site, leading to widening of the pores at higher fluence [315]. At higher resolution FESEM images, a decrease in the diameter of the nanotubes is observed with the increase in the irradiation fluence to 1.3×10^{13} ions cm^{-2} [Figure 5.1 (g)] as compared to that of the pristine nanocomposite [Figure 5.1 (f)], which is also confirmed from HRTEM micrographs as shown in Figure 5.2. The average diameter of the nanotubes decreases from 132 nm for pristine nanocomposite to 117 nm upon irradiating with the fluence of 2.2×10^{12} ions cm^{-2} as evident from Figure 5.2 (a) and 5.2 (b). Also, broken nanotubes could be observed at a fluence of 2.2×10^{12} ions cm^{-2}. However, at the highest fluence of 1.3×10^{13} ions cm^{-2}, though a porous surface is visible from FESEM image, HRTEM micrograph demonstrates highly fragmented and degraded nanotubes. The passage of energetic ions creates a cylindrical disordered zone along its path resulting in disorder ranging from point defects to a continuous amorphized zone [203]. At low fluences, the induced damage is low but beyond a certain fluence, the nanotubes in the composite electrode become unstable and get fragmented. Thus, SHI irradiation results in a significant change in the morphology and porosity of the nanocomposite electrode.

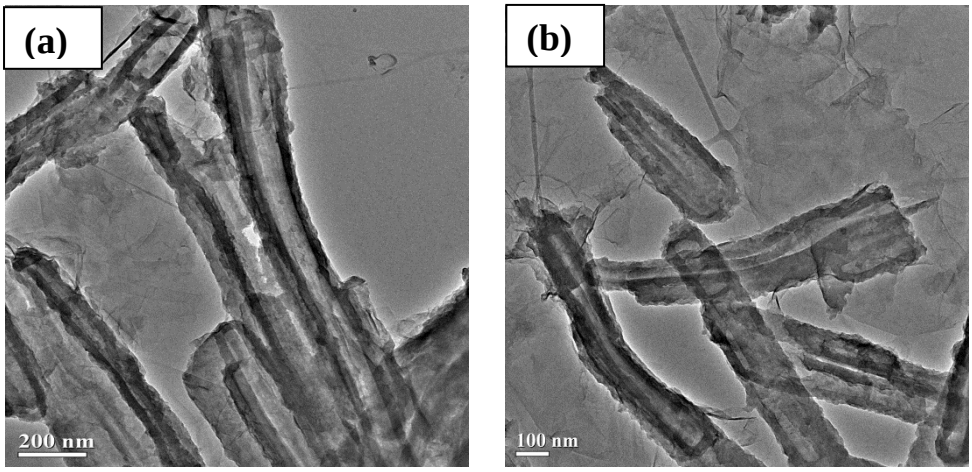

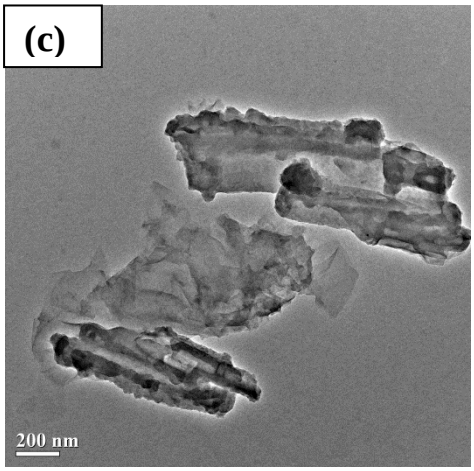

Figure 5.2: *HRTEM micrographs of 40 wt. % RGO-PPyNTs nanocomposite (a) pristine, and irradiated with fluence of (b) 2.2 × 10^{12} and (c) 1.3 × 10^{13} ions cm^{-2}.*

5.2.2 X-ray diffraction analysis

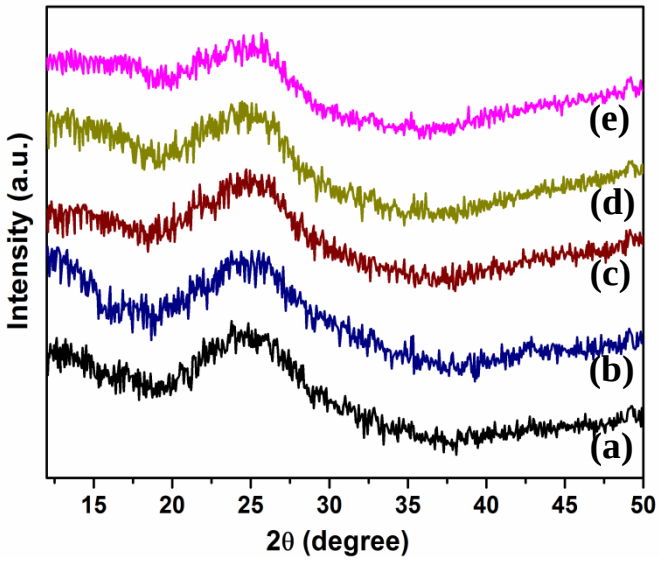

Figure 5.3: *X-ray diffractograms of 40 wt. % RGO-PPyNTs nanocomposite (a) pristine, and irradiated with fluence of (b) 6 × 10^{10}, (c) 3.6 × 10^{11}, (d) 2.2 × 10^{12} and (e) 1.3 × 10^{13} ions cm^{-2}.*

The XRD patterns of pristine and 85 MeV C^{6+} SHI irradiated 40 wt. % RGO-PPyNTs nanocomposites are shown in Figure 5.3. A prominent broad peak in the 2θ range of 19°-30° is observed in the XRD patterns, which is attributed to overlapping of the diffraction peak of RGO and PPyNTs and implies semi-crystalline nature of the nanocomposite system. The semi-crystalline nature of the nanocomposite system

may result from exfoliated RGO nanosheets and local ordering of the polymer chains by chain folding or by the formation of single or multiple helices along their length [316]. It is observed that with increase in ion fluence, there is not much change in the intensity of the peaks up to a fluence of 2.2×10^{12} ions cm^{-2}. This suggests that the material crystallinity is not significantly affected by an ion dose till 2.2×10^{12} ions cm^{-2}. On further increase in fluence, the sample peak intensity decreases indicating a decrease in the crystallinity of the sample. The relative crystallinity percentage of pristine and irradiated nanocomposites with increasing fluence has been calculated to be 33.2, 32.3, 32.7, 32.1 and 28.4% using equation (3.7). The decline in crystallinity at the highest fluence may be ascribed to the decrease in the local ordering and chain scission of polymer chains at high irradiation dose of 1.3×10^{13} ions cm^{-2}. At low fluence, the energy deposition is not sufficient enough to vary the overall crystallinity of the material contributed by both RGO and PPyNTs. At a high fluence of 1.3×10^{13} ions cm^{-2}, the irradiated tracks overlap and the damage produced in the cylindrical disordered zone at each ion impact site starts to dominate contributing to primary amorphous zone generation resulting in the crystallinity decrease in the nanocomposite.

5.3 Vibrational spectroscopy

5.3.1 Fourier transform infrared spectroscopy

The FTIR spectra of pristine and irradiated 40 wt. % RGO-PPyNTs nanocomposites are displayed in Figure 5.4. The FTIR spectrum of pristine nanocomposite depicts the peaks at wavenumbers 3442, 1557, 1475, 1312, 1197, 1037 and 927 cm^{-1} as discussed in Chapter 4. The 1557 and 1475 cm^{-1} bands correspond to C=C stretching and C-N stretching vibrations of the pyrrole ring, respectively [280]. These characteristics peaks of PPyNTs are observed to weaken upon irradiation with the highest fluence of 1.3×10^{13} ions cm^{-2}, which is due to bond-breaking or chain scissioning of the main chain of PPyNTs. The peaks at 1312 and 1037 cm^{-1} are assigned to C-H in-plane stretching vibrations of PPyNTs, respectively [281]. The absorptions at 1197 and 927 cm^{-1} represent the doped states of PPyNTs [282]. The C=C stretching vibration of RGO appears as a weak shoulder at 1628 cm^{-1} in the pristine nanocomposite. Upon irradiation at the fluence of 6×10^{10} ions cm^{-2}, the 1628 cm^{-1} peak of RGO is intensified as compared to that of pristine nanocomposite

indicating an increased contribution of C=C stretching vibration of RGO for the 6 × 10^{10} ions cm^{-2} irradiated nanocomposite. The broad absorption band centered at around 3442 cm^{-1} in the nanocomposite corresponds to the overlapping of the O-H and N-H stretching vibrations of RGO and PPyNTs at 3438 and 3416 cm^{-1}, respectively [285, 286]. The small peaks at 2853 and 2924 cm^{-1} are attributed to the CH and CH_2 stretching, respectively in both RGO and PPyNTs [287]. Table 5.1 presents the IR bands of 40 wt. % RGO-PPyNTs nanocomposite along with their respective positions.

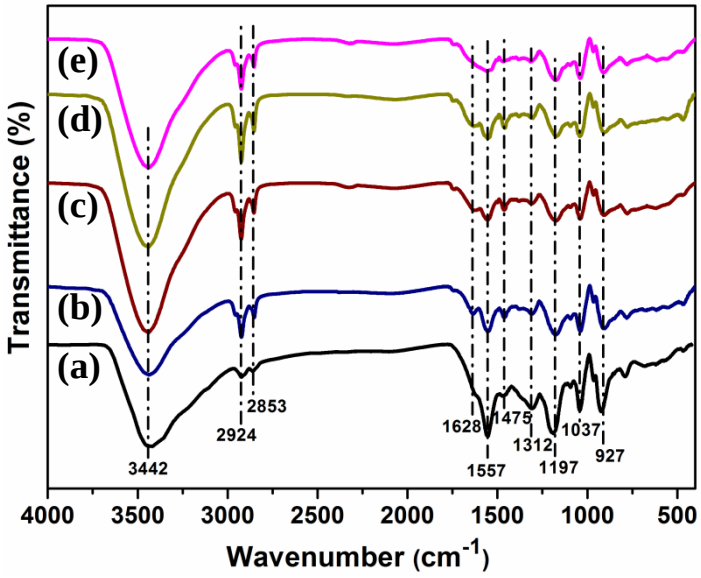

Figure 5.4: *FTIR spectra of 40 wt. % RGO-PPyNTs nanocomposite (a) pristine, and irradiated with fluence of (b) 6 × 10^{10}, (c) 3.6 × 10^{11}, (d) 2.2 × 10^{12} and (e) 1.3 × 10^{13} ions cm^{-2}.*

Table 5.1: *Characteristic IR bands of 40 wt. % RGO-PPyNTs nanocomposite and their assignments*

IR Bands	**Assignments**
927, 1197 cm^{-1}	Doped states of PPyNTs [282]
1037, 1312 cm^{-1}	C-H in-plane stretching [281]
1475 cm^{-1}	C-N stretching [280]
1557 cm^{-1}	C=C stretching of PPyNTs [280]
1628 cm^{-1}	C=C stretching of RGO [283]
2853, 2924 cm^{-1}	CH and CH_2 stretching [287]
3442 cm^{-1}	Overlapping of O-H and N-H stretching vibrations

5.3.2 Micro-Raman spectroscopy

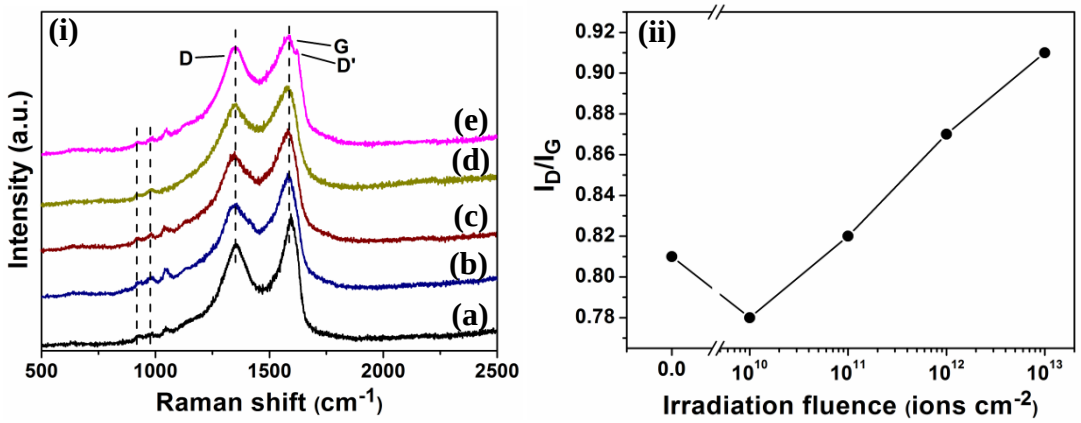

Figure 5.5: *(i) Micro-Raman spectra of 40 wt. % RGO-PPyNTs nanocomposite (a) pristine, and irradiated with fluence of (b) 6 × 10^{10}, (c) 3.6 × 10^{11}, (d) 2.2 × 10^{12} and (e) 1.3 × 10^{13} ions cm^{-2}; (ii) Variation of disorder parameter (I_D/I_G) with irradiation fluence.*

Micro-Raman spectroscopy has been conducted to study the molecular vibrations as well as the introduction of defects. Figure 5.5 (i) depicts the evolution of the Raman spectrum of 40 wt. % RGO-PPyNTs nanocomposite with increasing fluence of 85 MeV C^{6+} SHI irradiation. The μ-Raman spectra of the nanocomposite show peaks at 922, 982, 1355 and 1595 cm^{-1}. The small peaks at 922 and 982 cm^{-1} correspond to the doped states of PPy associated with ring deformation of dication and radical cation, respectively [294]. The other two bands that appear for PPyNTs at 1382 and 1588 cm^{-1} due to ring stretching vibration and π conjugated structure [292] is found to overlap with the bands of RGO at 1355 and 1595 cm^{-1}, respectively. Two prominent peaks are observed in the μ-Raman spectra of the nanocomposites: D peak at 1355 cm^{-1} and G peak at 1595 cm^{-1}. The G band is assigned to the E_{2g} phonon mode of sp^2 hybridized carbon atoms, the D band is attributed to the A_{1g} symmetry phonons near the K-zone boundary and indicates the presence of amorphous or disordered carbon in the material [317]. A band, known as D' at 1621 cm^{-1} is also observed for the highest irradiated sample, which represents a defect induced peak originating via an intra-valley double resonance process in the presence of defects [318]. The intensity ratio of the D and G bands (I_D/I_G), known as the disorder parameter, is used to study the structural disorder induced in a carbon nanostructure and can be applied for both RGO and PPyNTs [288, 319]. The

disorder parameter is plotted with irradiation fluence to quantitatively study the modifications induced in the nanocomposites by irradiation and shown in Figure 5.5 (ii). It is observed that with increasing irradiation fluence, the disorder parameter decreases at a fluence of 6×10^{10} ions cm^{-2} and starts increasing with increasing fluences up to 1.3×10^{13} ions cm^{-2}. The initial decrease in disorder parameter may be ascribed to the annealing or ordering of carbon atoms in RGO at moderate temperatures that occurs at a low fluence of 6×10^{10} ions cm^{-2} due to the energy dissipated by the incident energetic ions [320]. This ordering of RGO could be correlated with the intensified C=C stretching vibration at 1628 cm^{-1} as observed in the FTIR spectra of the 6×10^{10} ions cm^{-2} irradiated nanocomposite. This is further corroborated with the HRTEM results at that fluence where no significant damage is observed in the morphology of RGO and PPyNTs. With increasing fluence, the disorder parameter increases, which might be due to induced defects and distortions in the nanocomposites. This occurs because defect sites increase in the nanocomposite as the energy loss of SHI is high enough to dominate over the energy loss required for annealing [320]. At the highest fluence of 1.3×10^{13} ions cm^{-2}, the disorder parameter is highest indicating the increased density of defects and structural damage. This could be related to the chain scission of polymer chains at the fluence of 1.3×10^{13} ions cm^{-2} resulting in decomposed PPyNTs as evident from HRTEM micrograph. The appearance of D' band in the μ-Raman spectra at this fluence also supports the fact and indicates increased disorder in RGO. The characteristic micro-Raman peaks of 40 wt. % RGO-PPyNTs nanocomposite with their corresponding peak positions have been assigned in Table 5.2.

Table 5.2: *Characteristic micro-Raman bands of 40 wt. % RGO-PPyNTs nanocomposite and their assignments*

Raman Bands	**Assignments**
922, 982 cm^{-1}	Ring deformation of dication and radical cation [294]
1355 cm^{-1}	D band: breathing mode from sp^2 carbon rings [288, 317]
1382 cm^{-1}	Ring stretching mode [292]
1588 cm^{-1}	Stretching of π conjugated structure [292]
1595 cm^{-1}	G band: in-plane sp^2 C-C stretching [289, 317]
1621 cm^{-1}	D' band: arise due to double resonance intra-valley process

	in presence of defects [318]

5.4 Thermogravimetric analysis

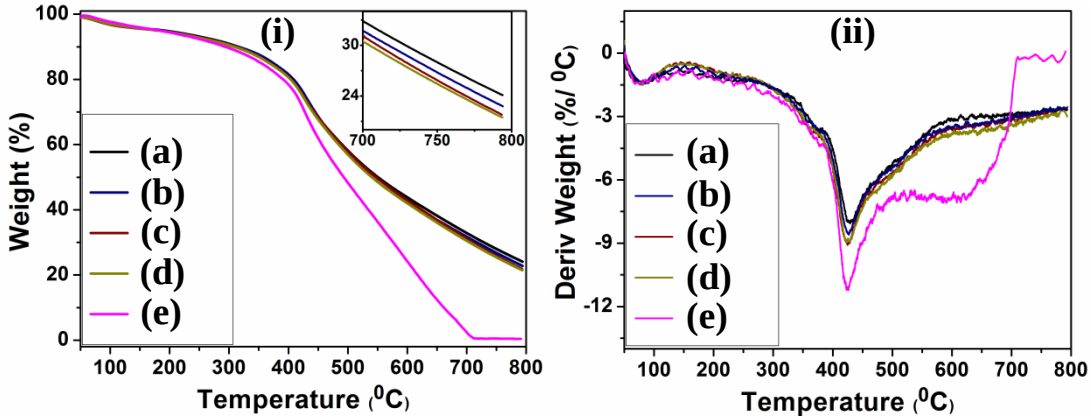

Figure 5.6: *(i) TG curves (Inset shows magnified TG curves) and (ii) derivative of TG curves of 40 wt. % RGO-PPyNTs nanocomposite (a) pristine, and irradiated with fluence of (b) 6 × 10^{10}, (c) 3.6 × 10^{11}, (d) 2.2 × 10^{12} and (e) 1.3 × 10^{13} ions cm^{-2}.*

Thermogravimetric analysis was carried out to investigate the thermal stability of pristine and irradiated 40 wt. % RGO-PPyNTs nanocomposites in the temperature range of 50-800 °C and the results are displayed in Figure 5.6 (i). The thermal degradation patterns of pristine and irradiated nanocomposites follow a two-step degradation process. The initial weight loss in the range of 50-110 °C is due to the removal of trapped moisture from the nanocomposites. The onset of major weight loss in the pristine nanocomposite is observed around 300 °C, which is attributed to thermal decomposition of the main chain of polypyrrole, as RGO is thermally stable and does not exhibit degradation within this temperature range. Upon SHI irradiation, a slight decrease in thermal decomposition temperature of the nanocomposites is observed, which indicates a decline in thermal stability of the samples with increasing fluence. The nanocomposite irradiated at the highest fluence of 1.3 × 10^{13} ions cm^{-2} suffers a rapid degradation and is completely carbonized around 700 °C with no residue left at 800 °C. Consequently, a mass loss of 100% is recorded for the highest irradiated nanocomposite as compared to 75.91% for that of the pristine nanocomposite at 800 °C. The dramatic weight loss at the highest fluence of 1.3 × 10^{13} ions cm^{-2} indicates the fast decomposition of the

nanocomposite, which could be ascribed to the highly defective RGO and fragmented PPyNTs caused by the large electronic energy loss of SHI at this fluence.

To clearly assess the thermal behavior of the nanocomposites, the derivative thermographs of TG curves for pristine and irradiated nanocomposites have been shown in Figure 5.6 (ii) and the onset decomposition (T_{onset}) and rapidest decomposition (T_{rpd}) temperatures for the major degradation measured from the plots have been summarized in Table 5.3. The TG derivative curves of all the samples display two peaks that imply two different degradations of adsorbed moisture and the PPy backbone, respectively. The rapidest temperatures of irradiated nanocomposites exhibit a gradual decrease with increasing irradiation fluence, which indicates an increase in degradation rate of the nanocomposites. The degradation is comparatively fast at the highest fluence of 1.3×10^{13} ions cm^{-2}, which is evident from the broad third derivative peak appearing in the range of 550-650 °C in the nanocomposite. This decrease in thermal stability of the nanocomposite may be attributed to introduction of defects and distortions in the nanocomposite structure by SHI at the fluence of 1.3×10^{13} ions cm^{-2}. The increased defect density of RGO and highly fragmented nanotubes at the fluence of 1.3×10^{13} ions cm^{-2} has been corroborated by Raman and HRTEM results. Defects in the structure are surrounded by weaker bonds, which reduce the mechanical strength and thermal stability of the material [321]. Hence SHI irradiation results in a decrease in thermal stability of the nanocomposites with increasing fluence, which is most pronounced at the highest fluence.

Table 5.3: *T_{onset}, T_{rpd} and % of degradation at 800 °C of pristine and irradiated 40 wt. % RGO-PPyNTs nanocomposites with different fluences*

Sample	T_{onset} (°C)	T_{rpd} (°C)	Degradation at 800 °C (%)
Pristine	304	429	75.91
6×10^{10}	304	426	77.24
3.6×10^{11}	304	425	78.12
2.2×10^{12}	304	425	78.46
1.3×10^{13}	268	424	100

5.5 Current-voltage (I-V) characteristics

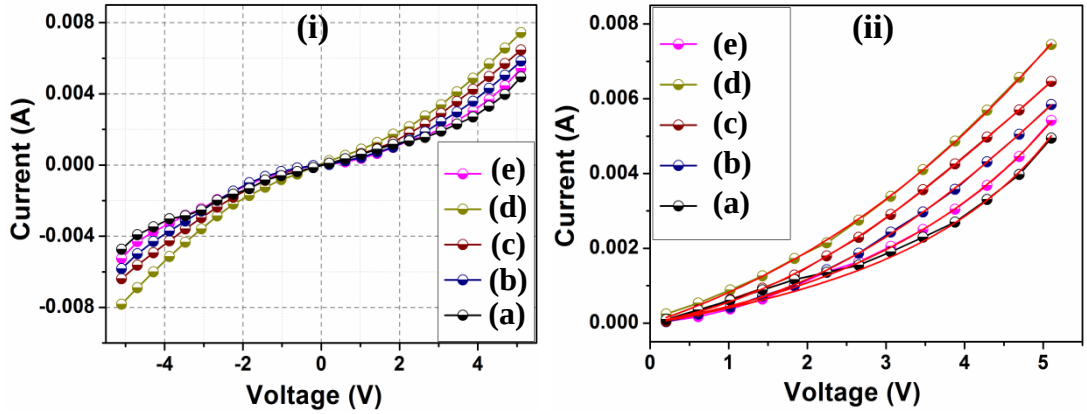

Figure 5.7: *(i) I-V characteristics and (ii) Kaiser equation fitted I-V curves of 40 wt. % RGO-PPyNTs nanocomposite (a) pristine, and irradiated with fluence of (b) 6 × 10^{10}, (c) 3.6 × 10^{11}, (d) 2.2 × 10^{12} and (e) 1.3 × 10^{13} ions cm^{-2}.*

The I-V characteristics for pristine and irradiated 40 wt. % RGO-PPyNTs nanocomposites are shown in Figure 5.7 (i). It is observed that the I-V characteristic curves follow a non-linear behavior that is symmetric with change in the polarity of the applied voltage. The non-linear nature of the I-V curves persists with increase in irradiation fluence, which indicates the same charge transport mechanism of charge carrier hopping along the polymer chain. The presence of RGO enhances the charge carrier motion in the nanocomposite by acting as a "conduction link" within the polymer matrix. This field dependent non-linear behavior of I-V curves can be explained with the help of Kaiser equation, which is given by:

$$G = \frac{I}{V} = \frac{G_0 \, exp(^{V}/_{V_0})}{1 + h[exp(^{V}/_{V_0}) - 1]} \tag{5.1}$$

where G_0 is the temperature-dependent low-field conductance (for V tends to zero), $h = {}^{G_0}/_{G_h}$ (where $h < 1$) exhibits a decrease in the G value below the exponential increase at higher voltages V and V_0 (depends strongly on barrier energy) measures the voltage scale factor that yields an exponential increase in conductance with increase in V. As the I-V curves are symmetric with respect to the polarity change, only the positive sides of I-V characteristics are considered for fitting according to equation (5.1), which are shown in red solid lines in Figure 5.7 (ii) and the fitting parameters are presented in Table 5.4. A slight increase in the value of low field

conductance (G_0) and parameter h is noticed as the ion dose increases up to 2.2 × 10^{12} ions cm^{-2}. This implies reduced non-linearity in the I-V curves with increasing fluence. An increment in the value of voltage scale factor (V_0) with increasing fluence is also observed, which reflects the decrease in non-linearity [322]. The decreased non-linearity indicates reduced hopping barriers within the polymer matrix till an ion dose of 2.2 × 10^{12} ions cm^{-2}. With further increase in fluence, all the parameters G_0, h and V_0 decrease implying increased resistance in charge carrier motion. This may be attributed to the increased defect density in RGO and complete fragmentation of nanotubes at a fluence of 1.3 × 10^{13} ions cm^{-2}.

Table 5.4: *Fitting parameters to Kaiser equation for pristine and irradiated 40 wt. % RGO-PPyNTs nanocomposites with different fluences*

Sample	G_0(S)	V_0 (V)	h
Pristine	9.4 × 10^{-4}	3.12	0.90
6 × 10^{10}	1.13 × 10^{-3}	3.58	0.92
3.6 × 10^{11}	1.57 × 10^{-3}	3.62	0.92
2.2 × 10^{12}	2.41 × 10^{-3}	3.81	0.94
1.3 × 10^{13}	9.9 × 10^{-4}	3.23	0.90

5.6 Conductivity measurements

Electrical conductivity of the pristine and SHI irradiated 40 wt. % RGO-PPyNTs nanocomposites with different fluences at room temperature has been calculated using equation (2.26). A slight increment in the conductivity values of the nanocomposites with increase in ion fluence up to 2.2 × 10^{12} ions cm^{-2} is observed, followed by a decline at a fluence of 1.3 × 10^{13} ions cm^{-2}. The conductivity values of pristine and irradiated nanocomposites with increasing fluences up to 1.3 × 10^{13} ions cm^{-2} are measured to be 4.47, 4.78, 5.89, 7.18 and 4.21 S cm^{-1}, respectively. The increase in conductivity upto a fluence of 2.2 × 10^{12} ions cm^{-2} signifies that the electrostatic interaction between RGO and PPyNTs is not affected by irradiation upto this fluence and the RGO-PPyNTs interfaces in the irradiated nanocomposites remain intact, where RGO provides conductive pathways for charge transfer in the nanocomposite. This is also corroborated by the FESEM and HRTEM images, where no significant change in the morphology of the irradiated nanocomposites is

observed till a fluence of 2.2×10^{12} ions cm^{-2} as compared to that of pristine nanocomposite except a change in the pore size. The improvement in conductivity upto a fluence of 2.2×10^{12} ions cm^{-2} could be attributed to the breaking of bonds in the target material that generates additional free charge carriers resulting in increased conductivity with increasing ion dose [323]. Increase in conductivity may also result from the removal of oxygen functional groups from the surface of RGO due to SHI irradiation, which causes evolution of gases from the target material. This occurs, however, in the initial stages of defect creation and does not seem to be applicable beyond a certain fluence. At a high fluence of 1.3×10^{13} ions cm^{-2}, increased defect density of RGO and chain scission of polymer chains may hinder the π-electron delocalization and weaken the electrostatic interaction between RGO and PPyNTs resulting in decreased conductivity. The decrease in diameter of the nanotubes, as evident from HRTEM micrographs, with increasing irradiation fluence may also contribute to the enhanced conductivity due to improved alignment of the nanotubes at a low diameter which may result in decreased resistivity in inter-chain electron hopping responsible for conduction between polymer chains. However, this does not apply at the highest fluence, where the nanotubes are completely degraded.

5.7 Surface area and pore size analysis

The specific surface area and pore size distribution of the pristine and irradiated 40 wt. % RGO-PPyNTs nanocomposites have been investigated by N_2 adsorption-desorption measurements at 77 K. The N_2 adsorption-desorption isotherms are shown in Figure 5.8 and the corresponding pore size distribution curves are shown in the inset. The specific surface areas have been calculated by the Brunauer-Emmett-Teller (BET) method from the adsorption data in the relative pressure (P/P_0) range of 0.05 to 0.35. The pristine RGO-PPyNTs nanocomposite displays a BET specific surface area of 208.4 $m^2\ g^{-1}$. The specific surface areas of the nanocomposites increase upon irradiation and are obtained to be 251.5 and 263.8 $m^2\ g^{-1}$ for irradiation fluence of 2.2×10^{12} and 1.3×10^{13} ions cm^{-2}, respectively. The total pore volume is estimated from a single point adsorption at a relative pressure of 0.95. The nanocomposites irradiated at the fluences of 2.2×10^{12} and 1.3×10^{13} ions cm^{-2} exhibit a pore volume of 0.491 and 0.531 $cm^3\ g^{-1}$, respectively which is larger than that of the pristine nanocomposite (0.377 $cm^3\ g^{-1}$). The pore size distributions are

obtained from the desorption data using the Barrett-Joyner-Halenda (BJH) method. From the pore size distribution curves, the pore size in the pristine nanocomposite is in the range of 1-9 nm with the peak value of the pore size distribution at ≈1 nm and ≈4 nm. For the irradiated nanocomposites at the fluences of 2.2×10^{12} and 1.3×10^{12} ions cm^{-2}, a broad pore size distribution is observed in the range of 4-30 nm and 6-50 nm where the peak centralizes at two areas with peak values of ≈4, ≈14 nm and ≈6, ≈21 nm, respectively. The increase in surface area and pore size is due to the damage tracks created by highly energetic SHI along its path, which is corroborated by the FESEM micrographs. Such a porous structure is beneficial for providing shorter electrolyte ion diffusion pathways resulting in the increase in electrochemically active sites in the nanocomposite films for enhanced charge storage.

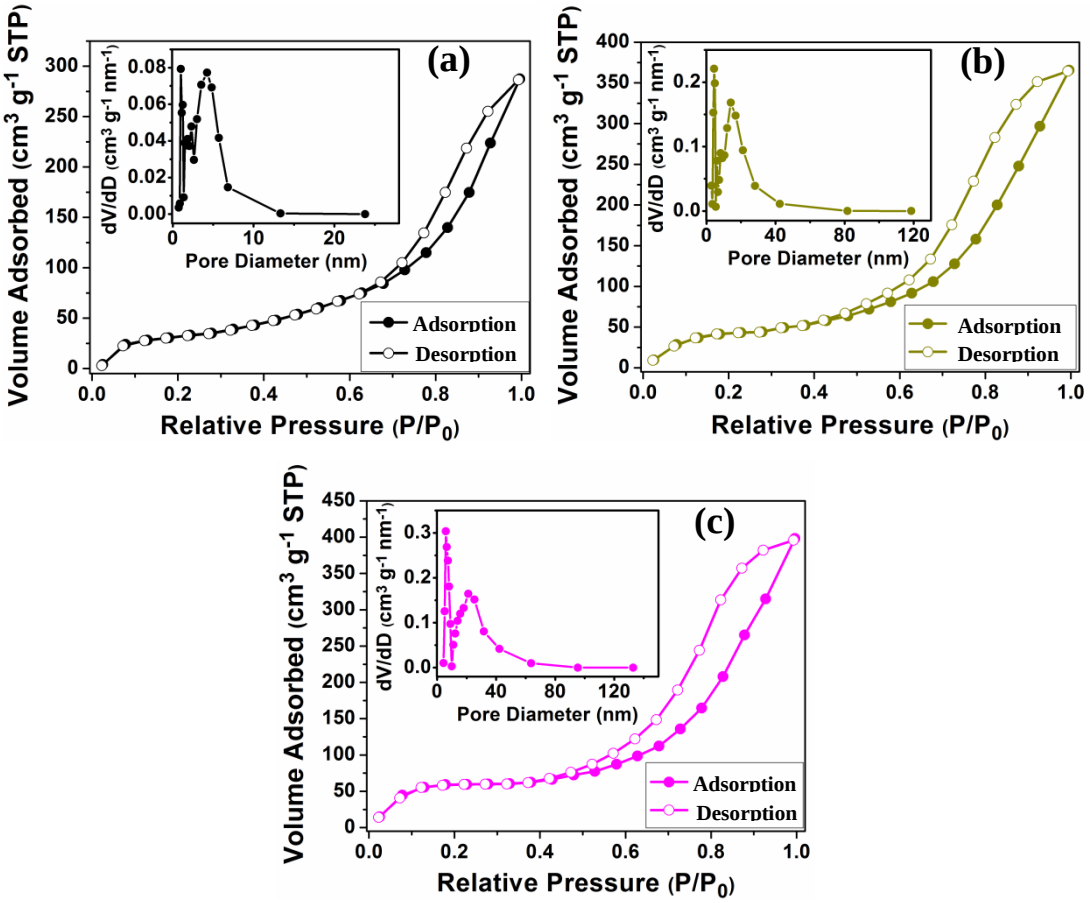

Figure 5.8: *N_2 adsorption-desorption isotherms of 40 wt. % RGO-PPyNTs nanocomposite (a) pristine, and irradiated with fluence of (b) 2.2×10^{12} and (c) 1.3×10^{13} ions cm^{-2}. The insets show the corresponding pore size distribution curves.*

5.8 Contact angle measurements

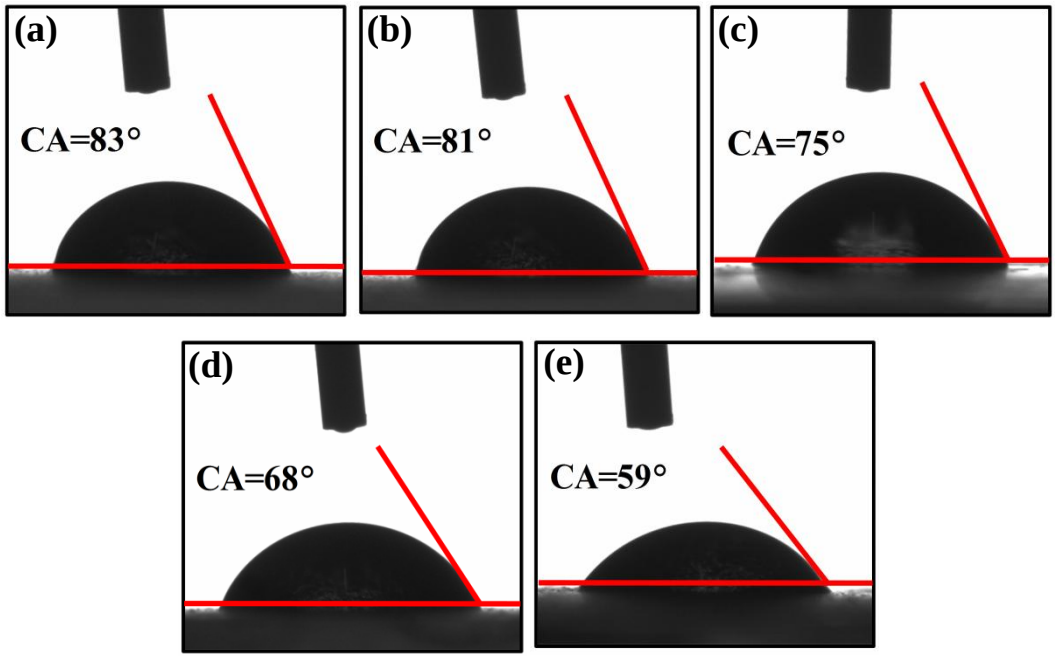

Figure 5.9: *Water contact angles of 40 wt. % RGO-PPyNTs nanocomposite (a) pristine, and irradiated with fluence of (b) 6 × 10^{10}, (c) 3.6 × 10^{11}, (d) 2.2 × 10^{12} and (e) 1.3 × 10^{13} ions cm^{-2}.*

Surface wettability of electrode is an essential parameter influencing the electrode-electrolyte reactivity. In order to study the degree of interaction between the electrode surface and an aqueous solvent, water contact angle measurements of the pristine and irradiated 40 wt. % RGO-PPyNTs nanocomposites have been conducted and shown in Figure 5.9. The water contact angle of pristine RGO-PPyNTs nanocomposite is measured to be 83°. Upon SHI irradiation, a decrease in the water contact angle of the nanocomposites with increasing fluence is observed. The decrease in contact angle of the irradiated nanocomposites as compared to that of pristine nanocomposite implies increase in wettability of the electrode surface upon irradiation. As surface wettability is directly related to the surface free energy, the Owens, Wendt, Rabel and Kaelble (OWRK) method have been used for calculation of total surface free energy to confirm the increased wettability. This method uses the contact angle values of two liquids, one polar (water) and other apolar (diiodomethane) for calculating the total surface energy in terms of polar and dispersive components using equation (2.73). The contact angles of water and diiodomethane and the calculated values of total surface energy with its polar and

dispersive components are presented in Table 5.5. It is clear from the table that the total surface energy of the nanocomposite electrodes increases with increase in irradiation fluence, which results in lower values of water contact angles of the irradiated nanocomposites. This indicates that SHI irradiation results in an increase in surface wettability of the nanocomposite electrode, which may result from enhanced specific surface area and pore size of the nanocomposites with increasing fluence of SHI irradiation.

Table 5.5: *Contact angles of water and diiodomethane, values of total surface energy (Υ_s^{Total}) and its polar (Υ_s^p) and dispersive (Υ_s^d) components of pristine and irradiated 40 wt. % RGO-PPyNTs nanocomposites obtained by OWRK method*

Sample	Water	Diiodomethane	Υ_s^d	Υ_s^p	Υ_s^{Total} (mNm^{-1})
Pristine	83	71	22.31	6.91	29.22
6×10^{10}	81	68	23.99	7.24	31.23
3.6×10^{11}	75	60	28.57	8.53	37.10
2.2×10^{12}	68	54	32.01	10.93	42.94
1.3×10^{13}	59	46	36.47	12.24	48.71

5.9 Electrochemical properties

5.9.1 Cyclic voltammetry

The CV curves of pristine and irradiated 40 wt. % RGO-PPyNTs nanocomposites recorded at different potential scan rates in 1 M KCl electrolyte in a potential range of –0.2 V to 0.8 V are presented in Figure 5.10.

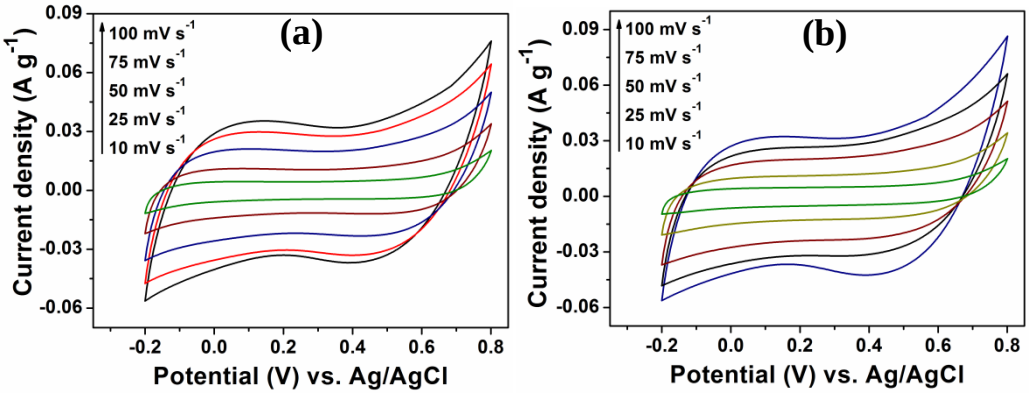

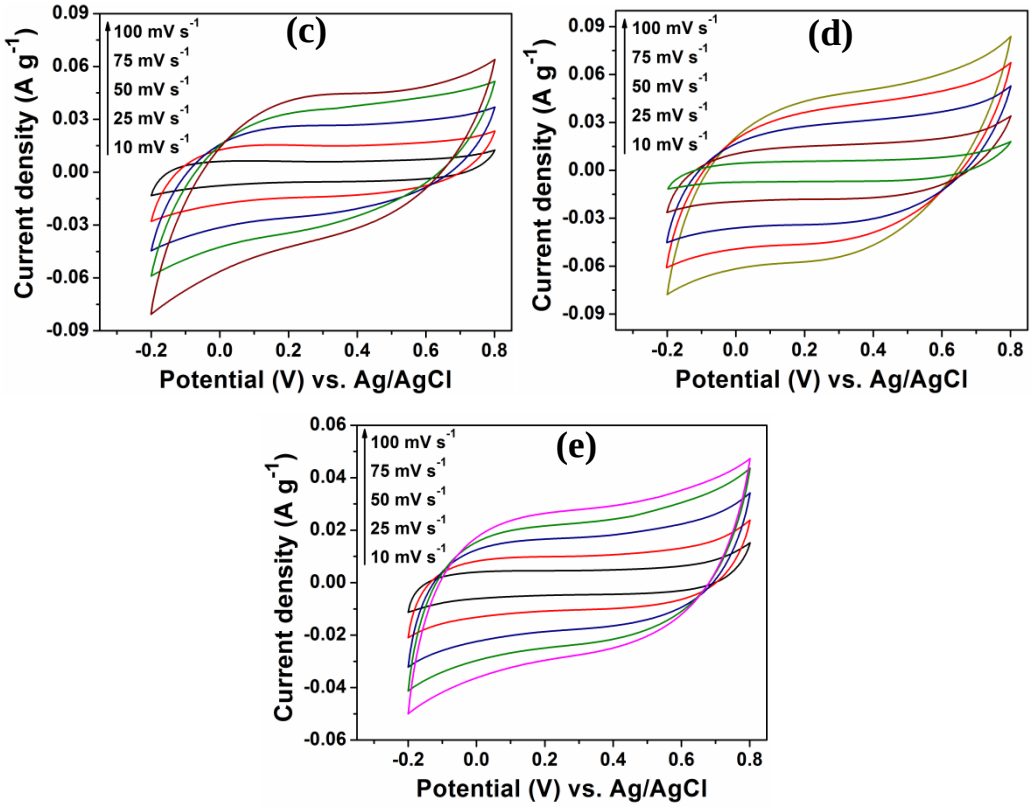

Figure 5.10: *CV curves at different voltage scan rate of 40 wt. % RGO-PPyNTs nanocomposite (a) pristine, and irradiated with fluence of (b) 6 × 10^{10}, (c) 3.6 × 10^{11}, (d) 2.2 × 10^{12} and (e) 1.3 × 10^{13} ions cm^{-2}.*

The CV curve of pristine nanocomposite exhibits a quasi-rectangular shape with a slight distortion, which implies the synergistic contribution of both EDLC and pseudocapacitance in the nanocomposites. The EDLC component is contributed by RGO, while PPyNTs exhibit pseudocapacitive behavior originating from reversible redox reactions on the electrode-electrolyte interface. In case of the irradiated nanocomposite, the current and area of the CV curves are found to increase with an increase in irradiation fluence up to 2.2 × 10^{12} ions cm^{-2}. The increased area and current of the CV curves indicate improved charge storage capacity of the nanocomposites upon irradiation. Moreover, a change in shape of the CV curves of the nanocomposites is noticed with increasing irradiation fluence. For the nanocomposite irradiated at a fluence of 6 × 10^{10} ions cm^{-2}, the CV curves do not show a significant variation from that of the pristine nanocomposite. However, with an increase in fluence to 3.6 × 10^{11} ions cm^{-2}, the CV curves deviate from quasi-rectangular shape to a non-rectangular 'leaf-like' shape. At the fluence of 2.2 × 10^{12}

ions cm^{-2}, the non-rectangular 'leaf-like' shape of the CV curve is more prominent and covers a larger area [Figure 5.10 (d)], which returns to the original quasi-rectangular shape at the highest fluence of 1.3×10^{13} ions cm^{-2} [Figure 5.10 (e)]. This transition in shape of the CV curves could be ascribed to the increase in surface area and porosity of the nanocomposites with increasing fluence as determined by BET and BJH analysis. The enhanced porosity at fluences of 3.6×10^{11} and 2.2×10^{12} ions cm^{-2} increase the electrochemically active sites of RGO and PPyNTs in the nanocomposites, which could not be accessed by the electrolyte ions in the pristine nanocomposite [99]. However, as the ratio of PPyNTs is high in RGO-PPyNTs nanocomposites, the contribution of pseudocapacitance in the nanocomposite arising from the faradaic reactions of active sites of PPyNTs increases, resulting in a non-rectangular 'leaf-like' CV shape, which is most pronounced at a fluence of 2.2×10^{12} ions cm^{-2}. At the highest fluence of 1.3×10^{13} ions cm^{-2}, the PPyNTs are highly fragmented and could no longer contribute to the doping-dedoping process resulting in a reduction in the area and current response of the CV curve giving rise to a decline in pseudocapacitance at this fluence. The CV curve therefore exhibits an improved rectangular shape indicating the dominant contribution of EDLC in the nanocomposite. The decreased diameter of PPyNTs with increasing fluence as observed from FESEM images may also lead to an increment in charge storage capacity as a result of increase in the overall available surface area of the nanocomposites to be accessible to the electrolyte ions. The improved conductivity of the electrode also contributes to enhanced current response in the nanocomposites.

5.9.2 Galvanostatic charge-discharge measurements

The GCD measurements of the nanocomposites have been conducted at a current density of 0.5 A g^{-1} in 1 M KCl electrolyte in the voltage range of 0-0.8 V. The first charge-discharge curves for pristine and irradiated 40 wt. % RGO-PPyNTs nanocomposites with different fluences are presented in Figure 5.11 (i). The charge-discharge curves of the pristine and irradiated nanocomposites show a nearly linear and symmetric discharge indicating capacitive behavior. On irradiation with increasing ion fluences, the discharge duration of RGO-PPyNTs nanocomposite is slightly prolonged as compared to that of pristine nanocomposite except for the highest fluence of 1.3×10^{13} ions cm^{-2}. This indicates an increase in specific

capacitance of the nanocomposites up to fluence of 2.2×10^{12} ions cm^{-2} followed by a decline at a fluence of 1.3×10^{13} ions cm^{-2}. The increase in porosity of the nanocomposites and decrease in the diameter of PPyNTs upon SHI irradiation gives rise to more electrochemically active sites in the electrode for charge storage resulting in enhanced specific capacitance. The specific capacitance (C_{sp}) and the coulombic efficiency (η) have been calculated using equations (2.41) and (2.32) and are presented in Table 5.6.

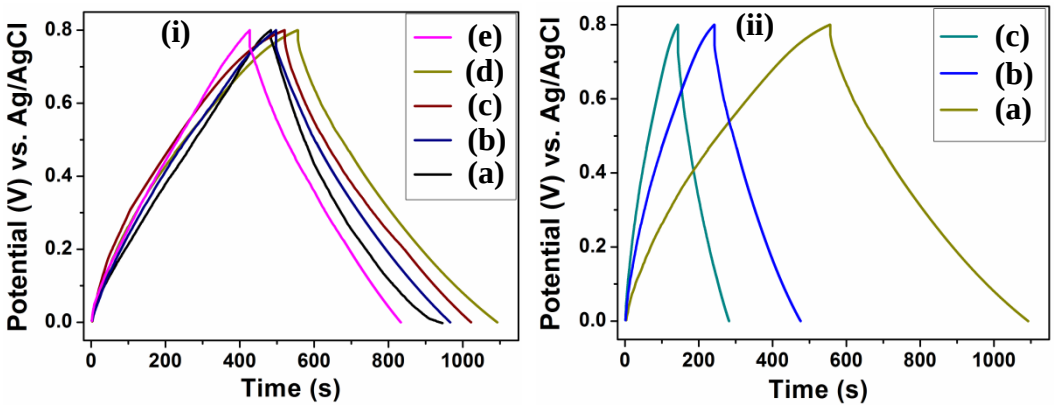

Figure 5.11: *(i) GCD curves of 40 wt. % RGO-PPyNTs nanocomposite (a) pristine, and irradiated with fluence of (b) 6×10^{10}, (c) 3.6×10^{11}, (d) 2.2×10^{12} and (e) 1.3×10^{13} ions cm^{-2} at a current density of 0.5 A g^{-1}; (ii) GCD curves of 2.2×10^{12} ions cm^{-2} irradiated RGO-PPyNTs nanocomposite at a current density of (a) 0.5 A g^{-1}, (b) 1 A g^{-1} and (c) 1.5 A g^{-1}.*

Table 5.6: *Specific capacitance, energy density, power density, coulombic efficiency, equivalent series resistance (R_s) and charge transfer resistance (R_{ct}) of pristine and irradiated 40 wt. % RGO-PPyNTs nanocomposites with different fluences*

Sample	**Specific capacitance ($F\ g^{-1}$)**	**Energy density ($W\ h\ kg^{-1}$)**	**Power density ($W\ kg^{-1}$)**	**Coulombic efficiency**	**R_s (Ω)**	**R_{ct} (Ω)**
Pristine	299.81	24.68	192.49	96%	6.95	4.6
6×10^{10}	308.64	25.41	192.35	96%	6.8	2.7
3.6×10^{11}	325.07	26.76	192.32	96%	6.61	2.2
2.2×10^{12}	346.28	28.51	192.39	96%	6.47	1.5
1.3×10^{13}	268.79	20.99	187.22	94%	6.95	4.42

The highest specific capacitance is found to be 346 F g^{-1} for the nanocomposite irradiated with an ion fluence of 2.2×10^{12} ions cm^{-2} and its GCD curves at different current densities are shown in Figure 5.11 (ii). High capacitance values are characterized by a developed surface area where the presence of pores is crucial [99]. Pores allow fast ionic diffusion across a densely packed bulk electrode in a short pathway and increase the available electrochemically active sites thus enhancing the capacitance [324]. It is noticed that the increase in capacitance is less at a low fluence of 6×10^{10} ions cm^{-2} and is comparatively high at intermediate fluences of 3.6×10^{11} and 2.2×10^{12} ions cm^{-2}. This could be related to the fact that the pores at low fluence contribute only to the adsorption of electrolyte ions, while at intermediate fluences, the pore size increases, which also allows the transportation of solvated ions from the electrolyte to the electroactive surfaces. The increase in surface wettability also contributes to the charge storage capacity of the irradiated nanocomposite by improving the interfacial electrode-electrolyte interaction. Moreover, the presence of defects to a small extent may also lead to rise in capacitance values. It is reported that defects create dangling bonds with a local charging that are receptive to adsorption and can assist the dissociation of adsorbates [325, 321]. Hence the minimal amount of induced defects and distortions in the material till an ion dose of 2.2×10^{12} ions cm^{-2}, as evident from Raman spectroscopy, may allow better access of electrochemically active sites of the electrode by facilitating the penetration of electrolyte ions resulting in enhanced charge storage. A small decrease in voltage (IR) drop of the nanocomposites with increasing fluence up to 2.2×10^{12} ions cm^{-2} suggests low overall resistance of the electrode. However, no further increase in capacitance is recorded as the fluence is increased to 1.3×10^{13} ions cm^{-2}. This might be ascribed to chain scissioning of the polymer chains and increased amorphicity of the polymer matrix at this fluence, though an increase in porosity is obtained from BJH analysis. Moreover, the increased defect density of RGO at the highest fluence of 1.3×10^{13} ions cm^{-2} as evident from the D' band of Raman spectra may also have a reverse effect in the capacitance of the nanocomposite. The energy density (E) and power density (P) values are calculated using the following equations:

$$E(Wh/kg) = \frac{1}{2} C_{sp} (\Delta V)^2 \tag{5.2}$$

$$P(W/kg) = \frac{E}{\Delta t_d} \tag{5.3}$$

where C_{sp} is the specific capacitance, Δt_d is the discharge time and ΔV is the discharge potential. The calculated values of energy density and power density are shown in Table 5.6. A high energy density of 28.51 W h kg^{-1} at a power density of 192.39 W kg^{-1} is achieved for the nanocomposite irradiated at a fluence of 2.2 × 10^{12} ions cm^{-2}.

5.9.3 Electrochemical impedance spectroscopy

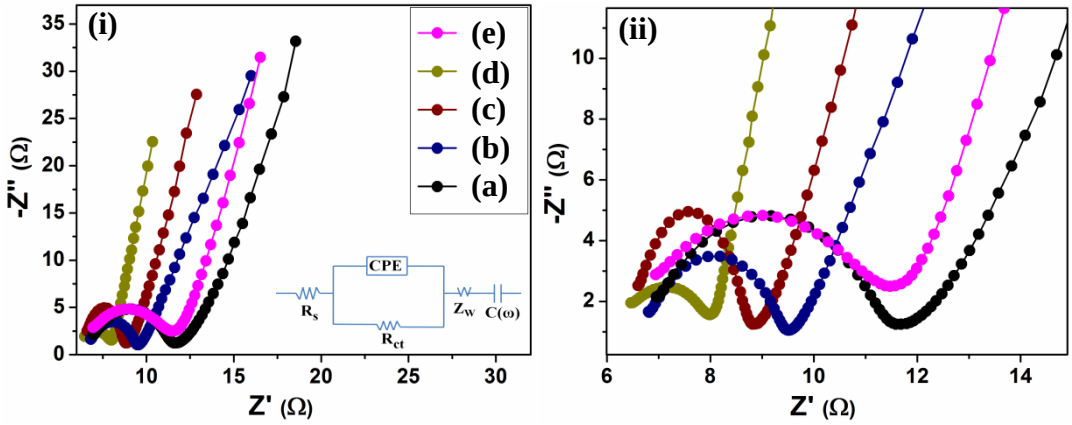

Figure 5.12: *(i) Nyquist plots of 40 wt. % RGO-PPyNTs nanocomposite (a) pristine, and irradiated with fluence of (b) 6 × 10^{10}, (c) 3.6 × 10^{11}, (d) 2.2 × 10^{12} and (e) 1.3 × 10^{13} ions cm^{-2} (Inset shows equivalent circuit) and (ii) Magnified view of the Nyquist plot in Z' range of 6-15 Ω.*

The interfacial resistive processes of the pristine and irradiated 40 wt. % RGO-PPyNTs nanocomposite electrodes have been studied by EIS in the frequency range of 10 mHz to 50 kHz at room temperature. The Nyquist plots of the pristine and irradiated nanocomposites with different fluences are shown in Figure 5.12 (i). The impedance characteristics have been analyzed on the basis of a Randles equivalent circuit as shown in the inset of Figure 5.12 (i), where R_s, R_{ct} and CPE are the equivalent series resistance, charge transfer resistance and interface capacitance observed in the high frequency region of Nyquist plot. The low frequency cell behavior is represented by the Warburg impedance (Z_w) and the supercapacitor cell capacitance (C(ω)), respectively [236]. The magnified view of Nyquist plot is shown in the inset of Figure 5.12 (ii) and the values of R_s and R_{ct} for pristine and irradiated

nanocomposites are listed in Table 5.6. The equivalent series resistance, evaluated from the x-intercept of Nyquist plot associated with the resistance of electrolyte, intrinsic resistance of the active material and the contact resistance at the active material/current collector interface is found to decrease slightly with increase in irradiation fluence upto 2.2×10^{12} ions cm^{-2}. The charge transfer resistance, which is measured by the diameter of the semicircle, is found to decrease with increase in the irradiation fluence till 2.2×10^{12} ions cm^{-2}. This indicates easier charge transfer across the interface between the electrode and the electrolyte as the irradiation fluence increases. This might be ascribed to the increased conductivity and reduced contribution of resistance from faradaic redox processes and double layer capacitance at the interface due to widening of pores up to an increasing fluence of 2.2×10^{12} ions cm^{-2}. A 45° slope at the lower frequencies indicates Warburg impedance, which is related to the diffusion of electrolyte ions into the electrode [326]. A low 45° slope portion is noticed with increase in irradiation fluence which implies low variations in ion diffusion path lengths to and within the electrode. This might be due to the increased porosity of the electrode, which facilitates the transport of electrolyte ions within the electrode. Moreover, the increasing vertical shape of the line at lower frequencies with increasing fluence indicates capacitor-like behavior and improved charge storage up to a fluence of 2.2×10^{12} ions cm^{-2}. However, on further increase in fluence to 1.3×10^{13} ions cm^{-2}, a significant increase in R_s and R_{ct} is observed in spite of an increase in the porosity of the electrode. This could be attributed to fragmentation of PPyNTs and highly defective RGO induced by SHI irradiation at this fluence, which hinders both electronic and ionic charge carrier motion resulting in increased resistance.

5.9.4 Cyclic stability study

The cyclic stability of pristine and irradiated 40 wt. % RGO-PPyNTs nanocomposites has been tested by repeating the CV measurements in 1 M KCl electrolyte at a scan rate of 10 mV s^{-1} for 1000 cycles. The specific capacitance values of the pristine and irradiated nanocomposites have been calculated with increasing cycle number using equation (2.38) and are shown in Figure 5.13 (i). It is observed from the figure that pristine RGO-PPyNTs nanocomposite exhibits a capacitive retention of 77% after 1000 cycles, which increases for the

nanocomposites upon SHI irradiation. With increase in SHI fluence, the cyclic stability gradually increases and is found to be the highest at a fluence of 2.2×10^{12} ions cm^{-2} with a capacitive retention of 89%. The CV curves for 2.2×10^{12} ions cm^{-2} irradiated nanocomposite with increasing number of cycles up to 1000 cycles is shown in Figure 5.13 (ii). It is observed from the figure that no appreciable distortion occurs in the shape of CV curves after 1000 cycles, which indicates its good electrochemical reversibility as an electrode. This may be attributed to the enlarged pores of the nanocomposites as fluence increases, which provides more electrochemically active sites in the electrode to be exposed to the electrolyte ions and consequently, the decrease in capacitance is less with increasing cycles. Enhanced porosity also increases the cycle life by accommodating the volume change in the electrode due to swelling/shrinkage during faradaic charge transfer across the electrode/electrolyte interface. However, this occurs till the irradiation fluence of 2.2×10^{12} ions cm^{-2}, beyond which the cyclic stability decreases, which could be ascribed to the low stability of the electrode due to the high concentration of induced defects and structural damage by SHI at a fluence of 1.3×10^{13} ions cm^{-2}.

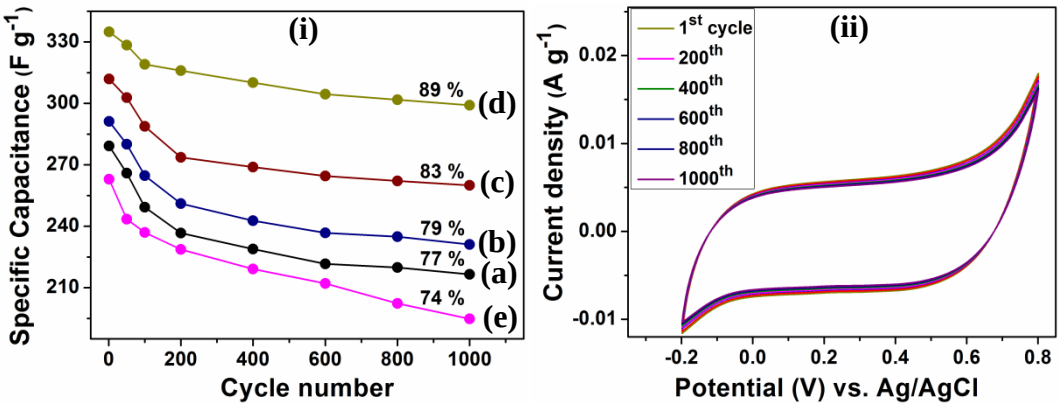

Figure 5.13: *(i) Variation of specific capacitance with cycle number of 40 wt. % RGO-PPyNTs nanocomposite (a) pristine, and irradiated with fluence of (b) 6×10^{10}, (c) 3.6×10^{11}, (d) 2.2×10^{12} and (e) 1.3×10^{13} ions cm^{-2}; (ii) CV curves with increasing cycle number of 40 wt. % RGO-PPyNTs nanocomposite irradiated at a fluence of 2.2×10^{12} ions cm^{-2}.*

5.10 Summary

Nanocomposite of RGO and PPyNTs with 40 wt. % of RGO has been irradiated with 85 MeV C^{6+} ions at four different fluences of 6×10^{10}, 3.6×10^{11}, 2.2×10^{12} and 1.3

$\times 10^{13}$ ions cm^{-2}. FESEM results reveal the widening of pores of the nanocomposite electrode with increasing irradiation fluence. HRTEM micrographs demonstrate decrease in the average diameter of PPyNTs from 132 nm for pristine nanocomposite to 117 nm for that of irradiated nanocomposite with fluence of 2.2×10^{12} ions cm^{-2}. In addition, fragmentation of PPyNTs is observed at the highest fluence of 1.3×10^{13} ions cm^{-2} from HRTEM images. XRD patterns indicate that the crystallinity of the nanocomposite is not affected till an irradiation dose of 2.2×10^{12} ions cm^{-2}, beyond which the crystallinity decreases from 32% to 28% at the highest fluence of 1.3×10^{13} ions cm^{-2}. FTIR spectra reveal the reduced intensity of C=C stretching and C-N stretching vibrations of the pyrrole ring upon irradiation at the highest fluence of 1.3×10^{13} ions cm^{-2}, which suggest chain-scission and bond-breaking of the main chain of PPyNTs. The disorder parameter (I_D/I_G) is evaluated from the Micro-Raman spectra, which is found to decrease at the initial fluence of 6×10^{10} ions cm^{-2} followed by an increase with increasing fluences upto 1.3×10^{13} ions cm^{-2}. This indicates annealing effects in the nanocomposite at a low fluence of 6×10^{10} ions cm^{-2} above which defects are induced attaining the highest density at the fluence of 1.3×10^{13} ions cm^{-2}. The high structural defects in the nanocomposite at the highest fluence of 1.3×10^{13} ions cm^{-2} is also evident from the appearance of another defect induced band at 1621 cm^{-1} known as D', which arises due to an intra-valley double resonance process in the presence of defects. TG curves reveal a slight decrease in thermal stability of the nanocomposite upon irradiation upto a fluence of 2.2×10^{12} ions cm^{-2}. A degradation of 78% upto 800 °C is recorded for the 2.2×10^{12} ions cm^{-2} irradiated nanocomposite as compared to 75% for that of the pristine nanocomposite. The nanocomposite irradiated at the highest fluence of 1.3×10^{13} ions cm^{-2} suffers a rapid degradation and is completely carbonized at 700 °C. The derivative TG curves display a slight decrease in rapidest decomposition temperature from 429 °C for the pristine nanocomposite to 425 °C for that of 2.2×10^{12} ions cm^{-2} irradiated nanocomposite beyond which the nanocomposites exhibit a fast degradation rate. The I-V characteristics of the pristine nanocomposite follow a non-linear behavior, which persists upon irradiation indicating the same charge transport mechanism of charge carrier hopping along the polymer chain. Conductivity measurements reveal a slight increase in conductivity upon irradiation with a maximum value of 7.18 S cm^{-1} at the fluence of 2.2×10^{12} ions cm^{-2} beyond which the conductivity decreases. The N_2 adsorption-desorption isotherms reveal an increase in BET specific surface area

from 208.4 m^2 g^{-1} to 263.8 m^2 g^{-1} and average pore size from 4 nm to 21 nm with increasing ion irradiation fluence upto 1.3×10^{13} ions cm^{-2}. An increase in surface wettability and surface free energy of the nanocomposite electrode is achieved upon irradiation, which is attributed to the enhanced specific surface area and porosity of the nanocomposites. CV curves exhibit improved current response and increased area of the nanocomposites upon irradiation upto a fluence of 2.2×10^{12} ions cm^{-2} followed by a decreased current response at higher fluence. With increasing SHI fluence upto 2.2×10^{12} ions cm^{-2}, the CV curves change from quasi-rectangular shape to non-rectangular 'leaf-like' shape that returns back to the original quasi-rectangular shape at the highest fluence of 1.3×10^{13} ions cm^{-2}. This transition and improved current response in the CV curves till a fluence of 2.2×10^{12} ions cm^{-2} are attributed to the enhanced specific surface area and porosity of the nanocomposites upon irradiation. The enhanced porosity increases the available electrochemically active sites of PPyNTs in the electrode for faradaic charge transfer giving rise to an increased pseudocapacitance resulting in a non-rectangular CV shape. At the highest fluence of 1.3×10^{13} ions cm^{-2}, PPyNTs are highly fragmented and could not contribute to the charge storage process leading to a decline in pseudocapacitance. This results in the dominant contribution of EDLC and a quasi-rectangular CV shape of the nanocomposite electrode at this fluence. GCD measurements display prolonged discharge duration of the nanocomposites with an increase in irradiation fluence upto 2.2×10^{12} ions cm^{-2}. A maximum specific capacitance of 346 F g^{-1} is obtained for the nanocomposite irradiated at a fluence of 2.2×10^{12} ions cm^{-2} as compared to 299 F g^{-1} for that of the pristine nanocomposite. The increase in capacitance is less at a low fluence of 6×10^{10} ions cm^{-2} and is comparatively high at intermediate fluences of 3.6×10^{11} and 2.2×10^{12} ions cm^{-2}. This is ascribed to the fact that the pores at low fluence contribute only to the adsorption of electrolyte ions, while at intermediate fluences, the pore size increases, which also allows the transportation of solvated ions from the electrolyte to the electroactive surfaces. The maximum energy density and power density values of 28 W h kg^{-1} and 192 W kg^{-1}, respectively are achieved for the nanocomposite irradiated at a fluence of 2.2×10^{12} ions cm^{-2}. The specific capacitance decreases to 268 F g^{-1} as the irradiation fluence increases to 1.3×10^{13} ions cm^{-2} due to increased amorphicity of the polymer matrix and enhanced defect density of RGO induced by SHI in the nanocomposite. A decrease in equivalent series resistance from 6.9 Ω to 6.4 Ω and charge transfer

resistance from 4.6 Ω to 1.5 Ω is achieved for the 2.2×10^{12} ions cm^{-2} irradiated nanocomposite as compared to that of the pristine nanocomposite. An increase in cyclic stability of the electrode is obtained from 77% for the pristine nanocomposite to 89% for the nanocomposite irradiated at a fluence of 2.2×10^{12} ions cm^{-2}, beyond which it decreases to 74% at the highest fluence of 1.3×10^{13} ions cm^{-2} used in the present work.